Available online at www.sciencedirect.com

SciVerse ScienceDirect

Geochimica et Cosmochimica Acta 77 (2012) 121–134

Geochimica et Cosmochimica Acta

www.elsevier.com/locate/gca

Calcite growth kinetics: Modeling the effect of solution stoichiometry

Mariëtte Wolthers [a,b,*], Gernot Nehrke [c], Jon Petter Gustafsson [d], Philippe Van Cappellen [e]

[a] Department of Earth Sciences, Faculty of Geosciences, Utrecht University, P.O. Box 80021, 3508 TA Utrecht, The Netherlands
[b] Department of Chemistry, University College London, 20 Gordon Street, London WC1H 0AJ, United Kingdom
[c] Alfred Wegener Institute for Polar and Marine Research, Am Handelshafen 12, 27570 Bremerhaven, Germany
[d] Department of Land and Water Resources Engineering, Royal Institute of Technology, Brinellvägen 28, 100 44 Stockholm, Sweden
[e] Department of Earth and Environmental Sciences, University of Waterloo, 200 University Avenue West, Waterloo, Ontario, Canada N2L 3G1

Received 18 February 2011; accepted in revised form 21 October 2011; available online 7 November 2011

Abstract

Until recently the influence of solution stoichiometry on calcite crystal growth kinetics has attracted little attention, despite the fact that in most aqueous environments calcite precipitates from non-stoichiometric solution. In order to account for the dependence of the calcite crystal growth rate on the cation to anion ratio in solution, we extend the growth model for binary symmetrical electrolyte crystals of Zhang and Nancollas (1998) by combining it with the surface complexation model for the chemical structure of the calcite–aqueous solution interface of Wolthers et al. (2008). To maintain crystal stoichiometry, the rate of attachment of calcium ions to step edges is assumed to equal the rate of attachment of carbonate plus bicarbonate ions. The model parameters are optimized by fitting the model to the step velocities obtained previously by atomic force microscopy (AFM, Teng et al., 2000; Stack and Grantham, 2010). A variable surface roughness factor is introduced in order to reconcile the new process-based growth model with bulk precipitation rates measured in seeded calcite growth experiments. For practical applications, we further present empirical parabolic rate equations fitted to bulk growth rates of calcite in common background electrolytes and in artificial seawater-type solutions. Both the process-based and empirical growth rate equations agree with measured calcite growth rates over broad ranges of ionic strength, pH, solution stoichiometry and degree of supersaturation.

1. INTRODUCTION

The effects of physico-chemical parameters, including temperature, pressure, pH, ionic strength, degree of supersaturation and the presence of inhibitors, on the precipitation of calcite have been studied extensively (see for example the review by Morse et al. (2007)). However, until recently the dependence of calcite growth rates on the solution stoichiometry has received limited attention (Tai et al., 2005; Nehrke et al., 2007; Perdikouri et al., 2009; Larsen et al., 2010; Stack and Grantham, 2010). This is remarkable given that (a) the compositions of most natural waters are highly non-stoichiometric with respect to calcium carbonate, and (b) a large body of work has shown that growth and dissolution rates of ionic minerals are markedly affected by the anion to cation concentration ratio in solution (Davies and Jones, 1955; Davies and Nancollas, 1955; Christoffersen and Christoffersen, 1979; Stubičar et al., 1990; Verbeeck and Devenyns, 1990, 1992; Zhang and Nancollas, 1992; Burke and Nancollas, 1999; Chernov et al., 2006; Rashkovich et al., 2006; Kowacz et al., 2007).

In a recent study, Nehrke et al. (2007) conducted single calcite crystal growth experiments at fixed pH (10.2) and two degrees of supersaturation while varying the Ca^{2+} to

* Corresponding author at: Department of Earth Sciences, Faculty of Geosciences, Utrecht University, P.O. Box 80021, 3508 TA Utrecht, The Netherlands. Tel.: +31 30 2535171; fax: +31 30 2532648.
E-mail address: m.wolthers@uu.nl (M. Wolthers).

0016-7037/$ - see front matter © 2011 Elsevier Ltd. All rights reserved.
doi:10.1016/j.gca.2011.11.003

CO_3^{2-} solution activity ratio over several orders of magnitude, from values smaller to larger than one. Their results unambiguously show that the growth rate is highest when the solution activity ratio, $r_{aq} = \{Ca^{2+}\}/\{CO_3^{2-}\}$, is close to one, and decreases with increasing or decreasing values of r_{aq} (Fig. 1a). The observed dependence of the growth kinetics of calcite on r_{aq} was interpreted using the kink growth theory for non-Kossel crystals. However, to explain the near-symmetric dependence of the growth rate on r_{aq} observed in Fig. 1a, the attachment frequencies of calcium and carbonate must be assumed to be of comparable magnitude. A similar behavior of the growth kinetics with respect to the aqueous cation to anion ratio was observed for calcium and magnesium oxalate (Chernov et al., 2006). However, as remarked by Nehrke et al. (2007), the assumption of comparable attachment frequencies of cations and anions is counter-intuitive, given the much slower water exchange kinetics of cations compared to anions (Nielsen, 1984). More recently, Larsen et al. (2010) and Stack and Grantham (2010) investigated the effect of r_{aq} on the step velocity of a calcite growth hillock using atomic force microscopy (AFM). Both groups observed a strong dependency of the velocities on solution stoichiometry. In addition, they found that the step velocities of the obtuse and acute sides of growth spirals were differently affected by r_{aq}.

There is general agreement that above pH 4 the growth and dissolution of calcite are controlled by surface reactions (Plummer et al., 1978; Reddy et al., 1981). Several authors have linked calcite dissolution rates (Van Cappellen et al., 1993; Arakaki and Mucci, 1995; Pokrovsky and Schott, 2002; Pokrovsky et al., 2005) and growth rates (Nilsson and Sternbeck, 1999) to the chemical structure of the mineral–solution interface predicted by surface complexation models. In particular, Nilsson and Sternbeck (1999) applied a surface complexation approach to model the crystal growth kinetics of calcite.

The calcite growth rates measured by Nilsson and Sternbeck were obtained for solution stoichiometries in the range $0.0003 < 1/r_{aq} < 0.5$. While the model presented by Nilsson and Sternbeck is able to reproduce their own experimental growth rates, it fails to do so for the measured growth rates of Nehrke et al. (2007) (Fig. 2). In fact, the model of Nilsson and Sternbeck does not produce a rate maximum in the vicinity of $r_{aq} = 1$, as observed by Nehrke and coworkers (Fig. 1a). This calls into question the general applicability of the rate equation proposed by Nilsson and Sternbeck, in particular when the solution ratio r_{aq} is smaller than 1.

In this paper, we derive a new process-based growth model for calcite, by combining the surface structural model for divalent metal carbonates of Wolthers et al. (2008) (Table 1) with the growth model for binary electrolyte crystals of Zhang and Nancollas (1998). The latter authors showed that the growth rate of a binary crystal from aqueous solution cannot be defined solely in terms of the ion activity product, but is also a function of the solution activity ratio. In particular, their model (hereafter referred to as the Z&N model) yields a growth rate maximum at a value of the solution activity ratio that directly depends on the relative attachment frequencies of the lattice ions to growth sites at the crystal surface. The Z&N model is extended here by explicitly accounting for the different molecular configurations of surface sites at the carbonate mineral–aqueous solution interface.

2. PROCESS-BASED CALCITE GROWTH MODEL

2.1. Conceptual approach

As starting point, we consider the growth model developed by Kossel (1930) for crystals with a simple cubic lattice growing through the incorporation of a single type of (molecular) growth units at distinct surface sites, for example kink sites and step edges. The degree of supersaturation for a so-called Kossel crystal is given by the ratio of the activity of the growth unit in solution and the corresponding solubility equilibrium value. The growth of an

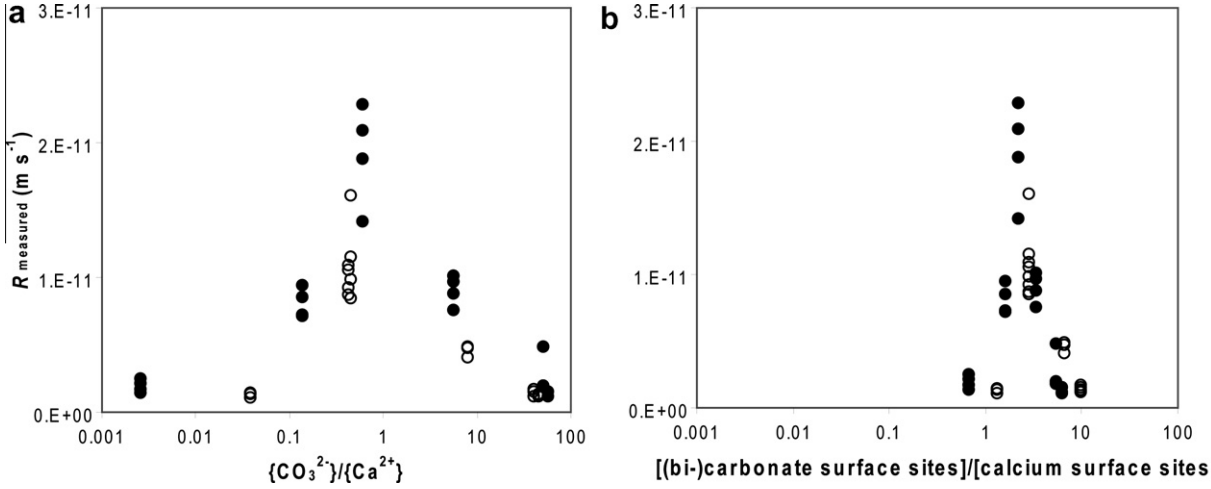

Fig. 1. Measured growth rates of single calcite crystals at $\Omega = 5.5 \pm 0.5$ (○) and $\Omega = 16 \pm 2$ (●) at pH 10.15 ± 0.05, 20 ± 0.2 °C and in the absence of a gas phase (Nehrke et al., 2007), plotted versus (a) the solution ion activity ratio and (b) the ratio of the surface density of carbonate plus bicarbonate sites over the surface density of calcium, sites calculated using the CD-MUSIC model (Table 1).

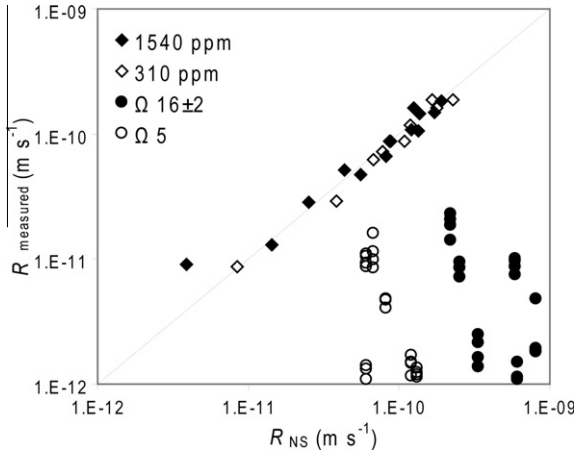

Fig. 2. Measured growth rates at 1540 ppm CO_2, $\Omega = 1.5$–8.3 (■) and 310 ppm CO_2, $\Omega = 1.7$–9.8 (□) (Nilsson and Sternbeck, 1999), and at $\Omega = 5$ (●) and $\Omega = 16 \pm 2$ (○) at pH 10.15 ± 0.05, 20 ± 0.2 °C and in the absence of a gas phase (Nehrke et al., 2007), plotted versus the model rates R_{NS} calculated using the growth model of Nilsson and Sternbeck (1999). For legibility, a solid line is plotted to indicate the $x = y$ relationship between the measured and modeled rates.

ionic crystal, such as NaCl, requires the alternating incorporation of cations and anions into the surface lattice. In this case, the growth rate is not only dependent on the saturation ratio Ω (with $\Omega = IAP/K_S$, where K_S is the solubility product and IAP is the activity product of the constituent ions), but also on the relative abundances of cations and anions in solution. Hence, several authors have extended the original Kossel model to describe the growth of multicomponent, ionic crystals (Nielsen, 1981; Zhang and Nancollas, 1998; Chernov et al., 2006).

In their growth model for ionic AB crystals, Zhang and Nancollas (1998) assume (among others) identical detachment frequencies for the cation and anion, a relatively low kink density so that nearby kink site interactions can be neglected, and negligible detachment from non-kink sites in supersaturated solutions. Based on these assumptions, they derive analytical solutions for the kink density, the kink nucleation rate, the rate of step movement, and the resulting growth rate of ionic AB crystals. In the development of the process-based model for calcite growth, we closely follow the approach of Zhang and Nancollas (1998).

The kinetic growth model for binary crystals is coupled to a recently developed surface model for divalent metal carbonate minerals (Wolthers et al., 2008; Table 1), based on the Charge Distribution MUltiSite Ion Complexation (CD-MUSIC) modeling approach of Hiemstra et al. (1996) and Hiemstra and Van Riemsdijk (1996). This model allows for variable proportions of face, edge and corner (or kink) sites exposed at the calcite surface. In addition, each of the structural sites can exhibit different chemical configurations that are described through the set of surface complexation reactions listed in Table 1. (Note that the set of reactions in Table 1 can be expanded when adsorbates other than the lattice ions are present in the aqueous medium.) In the CD-MUSIC model, charge across the electrical double layer (EDL) is distributed over three planes. This

Table 1
CD-MUSIC model tableau describing calcite surface chemistry (Wolthers et al., 2008). Subscript indexes c, e and f indicate corner, edge and face sites. Δz_0 and Δz_1 are Boltzmann parameters describing the charge distribution between the different planes across the mineral–solution interface (Hiemstra and Van Riemsdijk, 1996). Equilibrium constants obtained using a total of [a]2.2 and [b]2.4 accepting and donating hydrogen bridges (Wolthers et al., 2008); [c]from Van Cappellen et al. (1993).

	H^+	OH^-	Ca^{2+}	CO_3^{2-}	$\equiv_{c,e,f}CO_3H$	$\equiv_{c,e,f}CaOH$	$\log K$	Δz_0	Δz_1
Corner sites									
$\equiv_c CO_3^-$	−1				1		−3.58[a]	−1	0
$\equiv_c CO_3H_2^+$	1				1		−8.30[a]	+1	0
$\equiv_c CO_3Ca^+$	−1		1		1		−2.8[c]	−1	2[e]
$\equiv_c CaOH_2^+$	1					1	12.85[b]	+1	0
$\equiv_c CaO^-$	−1					1	−24.73[b]	−1	0
$\equiv_c CaHCO_3^0$	1	−1		1		1	10.15[c]	0.6	−0.6
$\equiv_c CaHCO_3^-$		−1		1		1	1.55[c]	0.6	−1.6
Edge sites									
$\equiv_e CO_3^{-2/3}$	−1				1		−3.58[a]	−1	0
$\equiv_e CO_3Ca^{+4/3}$	−1		1		1		−2.8[c]	−1[e]	2[e]
$\equiv_e CaOH_2^{+2/3}$	1					1	12.85[b]	+1	0
$\equiv_e CaO^{-4/3}$	−1					1	−24.73[b]	−1	0
$\equiv_e CaHCO_3^{-1/3}$	1	−1		1		1	10.15[c]	0.6	−0.6
$\equiv_e CaCO_3^{-4/3}$		−1		1		1	1.55[c]	0.6	−1.6
Face sites									
$\equiv_f CO_3^{-1/3}$	−1				1		−3.58[a]	−1	0
$\equiv_f CO_3Ca^{+5/3}$	−1		1		1		−2.8[c]	−1	2
$\equiv_f CaOH_2^{+1/3}$	1					1	12.85[b]	+1	0
$\equiv_f CaO^{-5/3}$	−1					1	−24.73[b]	−1	0
$\equiv_f CaHCO_3^{-2/3}$	1	−1		1		1	10.15[c]	0.6	−0.6
$\equiv_f CaCO_3^{-5/3}$		−1		1		1	1.55[c]	0.6	−1.6

Table 2
Proposed growth and dissolution reactions for the calcite surface, consistent with the thermodynamic calcite surface model of Table 1. k_{A_1}, k_{A_2}, k_{B_1}, k_{B_2} are attachment frequencies; ν_{A_1}, ν_{A_2}, ν_{B_1}, ν_{B_2} are detachment frequencies.

[3.1]	$\equiv_c CaCO_3^- + Ca^{2+}$	$\underset{\nu_{A_1}}{\overset{k_{A_1}}{\rightleftharpoons}}$	$\equiv_c CO_3Ca^+$
[3.2]	$\equiv_c CaHCO_3^0 + Ca^{2+}$	$\underset{\nu_{A_2}}{\overset{k_{A_2}}{\rightleftharpoons}}$	$\equiv_c CO_3Ca^+ + H^+$
[3.3]	$\equiv_c CO_3Ca^+ + CO_3^{2-}$	$\underset{\nu_{B_1}}{\overset{k_{B_1}}{\rightleftharpoons}}$	$\equiv_c CaCO_3^-$
[3.4]	$\equiv_c CO_3Ca^+ + HCO_3^-$	$\underset{\nu_{B_2}}{\overset{k_{B_2}}{\rightleftharpoons}}$	$\equiv_c CaHCO_3^0$

approach distinguishes between outer sphere complexes in the outermost plane and strongly bound surface ions.

The CD-MUSIC model for divalent metal carbonates has been calibrated against surface charge and potential measurements by adjustment of the number of hydrogen bridges between surface oxygen atoms and the number of water molecules in the interface (Wolthers et al., 2008). In the case of calcite, *a posteriori* testing against a large data set of different ζ-potential measurements and a sensitivity analysis indicated that (1) the CD-MUSIC model requires the accurate knowledge of the surface-site bond distances and number of hydrogen bridges, and (2) the validation of the model must be carried out with experimental data for which equilibrium between (clean) calcite surfaces, solution and gas phase is clearly demonstrated. A detailed discussion of the application of the CD-MUSIC model to calcite and its sensitivity to different parameters and assumptions is given in Wolthers et al. (2008).

Within the framework of the CD-MUSIC model description of the calcite–water interface, growth corresponds to the transfer of calcium and (bi-)carbonate ions from the outer to the inner region of the EDL, where they bind to (bi-)carbonate or calcium surface groups, respectively. (In what follows (bi-)carbonate refers to "carbonate plus bicarbonate".) In addition, the adsorbed ions preferentially incorporate into the lattice when binding to surface groups located in kink sites. Hence, calcite crystal growth can be represented by the four reactions given in Table 2. The reactions are assumed to be reversible and therefore account for both growth and dissolution of the mineral phase. It is important to note that the growth and dissolution reactions in Table 2 are internally consistent with the CD-MUSIC model, and that they are formulated so that during growth or dissolution the surface sites are continuously regenerated. Furthermore, the CD-MUSIC model is used to calculate the fraction, χ, of sites that represents growth sites at the calcite surface (Section 2.3).

In the derivation of the equations for calcite growth, we adopt most assumptions made by Zhang and Nancollas (1998). The assumption that the overall detachment frequencies for anions and cations are the same, however, does not hold for calcite as the net detachment frequency of (bi-)carbonate is related to the solubility product, as will be shown in the next section. We do assume that the theoretical approach for a cubic lattice is directly applicable to the rhombohedral calcite lattice. This assumption may be relaxed in future refinements of the model in order to account for AFM observations that show asymmetrical behavior of crystallographically distinct growth terraces (e.g., Teng et al., 2000; Stack and Grantham, 2010). A further implicit assumption is that the surface complexation reactions are rapid, relative to growth and dissolution. In other words, the chemical speciation of the calcite surface is assumed to remain at equilibrium.

Surface speciation calculations were carried out with the Visual Minteq software, modified to account for the existence of multiple surface sites (editions 2.60 β and 3.0; Gustafsson, 2008). Process-based growth model parameters and empirical rate equations were optimized using the MS Excel solver tool (Newton's method).

2.2. Equilibrium structure of the calcite step edge

The equilibrium and growth morphology of calcite is dominated by the $(10\bar{1}4)$ cleavage plane with obtuse and acute step edges (e.g., Stipp and Hochella, 1991; Paquette and Reeder, 1995; de Leeuw and Parker, 1998). Crystal growth occurs preferentially through the incorporation of the constituent ions, calcium and (bi-)carbonate, into the surface lattice at kink (or corner) sites along step edges (Nielsen and Toft, 1984). The following derivation of the process-based growth model therefore focuses on the fluxes of growth units in and out of kink sites.

For calcite, equilibrium is defined by the solubility product, K_S (Plummer and Busenberg, 1982):

$$K_S = \{Ca^{2+}\}_e\{CO_3^{2-}\}_e = \{A\}_e\{B_1\}_e = 10^{-8.48}(25^\circ C, 1\,bar) \quad (1)$$

where $\{Ca^{2+}\}_e$ and $\{A\}_e$ represent the activity of aqueous calcium, and $\{CO_3^{2-}\}_e$ and $\{B_1\}_e$ represent the activity of aqueous carbonate at equilibrium (index e). Note that we use activities when deriving the growth rate equation in order to be consistent with the model derivations of Zhang and Nancollas (1998) and to account for non-ideality effects experienced by aqueous species. There is no general agreement about whether to express rate laws in terms of activities or concentrations (Lasaga, 1998). Nielsen (1981), for instance, uses concentrations rather than activities in his non-Kossel growth equations. The solubility product K_S can be rewritten to one expressed in terms of the activities of calcium and bicarbonate (e.g., Hofmann et al., 2010):

$$K_{S_H} = \{Ca^{2+}\}_e\{HCO_3^-\}_e\{H^+\}^{-1} = \{A\}_e\{B_2\}_e 10^{-pH} = 10^{-1.85}\,(25^\circ C, 1\,bar) \quad (2)$$

where $\{HCO_3^-\}_e$ and $\{B_2\}_e$ represent the equilibrium activity of aqueous bicarbonate at equilibrium.

At equilibrium, the flux of calcium or (bi-)carbonate ions entering a given type of kink sites must be balanced by a corresponding outward flux. Considering the reactions in Table 2, we thus have:

$$k_{A_1}\{A\}_e\rho_{B_1} = v_{A_1}\rho_A, \quad (3)$$

$$k_{A_2}\{A\}_e\rho_{B_2} = k_{A_2}K_{\equiv CaHCO_3^0}10^{-pH}\{A\}_e\rho_{B_1} = v_{A_2}\rho_A, \quad (4)$$

$$k_{B_1}\{B_1\}_e\rho_A = v_{B_1}\rho_{B_1}, \quad (5)$$

$$k_{B_2}\{B_2\}_e\rho_A = k_{B_2}K_{HCO_3^-}10^{-pH}\{B_1\}_e\rho_A = v_{B_2}K_{\equiv CaHCO_3^0}10^{-pH}\rho_{B_1}, \quad (6)$$

where ρ_A, ρ_{B_1}, and ρ_{B_2} are the A-, B_1- and B_2-kink site densities, k_{A_1}, k_{A_2}, k_{B_1}, and k_{B_2} are the attachment frequencies of A, B_1 and B_2 ions, and v_{A_1}, v_{A_2}, v_{B_1}, and v_{B_2} are their detachment frequencies for the reactions defined in Table 2. The attachment of a calcium ion to a carbonate surface site is indicated by index A_1, that of calcium to a bicarbonate surface site by index A_2. Attachment of carbonate is indicated by index B_1 and attachment of bicarbonate is indicated by index B_2 (see also Fig. 3). The values of the equilibrium constants at 25 °C and 1 bar, are $K_{HCO_3^-} = 10^{10.33}$ (Plummer and Busenberg, 1982) and $K_{\equiv CaHCO_3^0} = 10^{8.6}$ (Table 1, Wolthers et al., 2008).

Combining Eqs. (3)–(6), leads to the following overall flux balances:

$$\bar{k}_A\{A\}_e\rho_{B_1} = \bar{v}_A\rho_A, \quad (7)$$

$$\bar{k}_B\{B_1\}_e\rho_A = \bar{v}_B\rho_{B_1}, \quad (8)$$

with

$$\bar{k}_A = k_{A_1} + K_{\equiv CaHCO_3^0}10^{-pH}k_{A_2}, \quad (9)$$

$$\bar{k}_B = k_{B_1} + K_{HCO_3^-}10^{-pH}k_{B_2}, \quad (10)$$

$$\bar{v}_A = v_{A_1} + v_{A_2}, \quad (11)$$

$$\bar{v}_B = v_{B_1} + K_{\equiv CaHCO_3^0}10^{-pH}v_{B_2}. \quad (12)$$

Eqs. (7) and (8) have exactly the same form as the flux balances derived by Zhang and Nancollas (1998, their equations [10] and [11]). Here, however, the pH dependency of the effective attachment and detachment frequencies ($\bar{k}_i, \bar{v}_j$) is explicitly accounted for via Eqs. (9)–(12).

Combining Eqs. (1), (7), and (8) leads to

$$K_S = \frac{\bar{v}_A\bar{v}_B}{\bar{k}_A\bar{k}_B}, \quad (13)$$

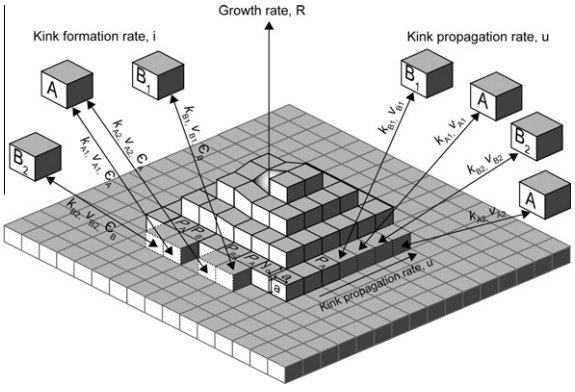

Fig. 3. Sketch to illustrate the concepts behind the process-based growth model. P_A, P_{B_1}, and P_{B_2} are the calcium, carbonate and bicarbonate growth sites; k_{A_1}, k_{A_2}, k_{B_1}, k_{B_2} are attachment frequencies; v_{A_1}, v_{A_2}, v_{B_1}, v_{B_2} are detachment frequencies; ε_A and ε_B are the energies to form an A or B kink site; a is the closest spacing between Ca^{2+} and CO_3^{2-} (3.199 Å); y_o is the step spacing.

Thus, once three of the effective frequencies are known, the fourth one is fixed through Eq. (13). From Eqs. (7) and (8), the ratio of kink densities ρ_A and ρ_{B_1} at equilibrium can be derived as follows:

$$\rho_A/\rho_{B_1} = r_i^{1/2}, \quad (14)$$

where r_i represents the kinetic ionic ratio:

$$r_i = \frac{\bar{k}_A\bar{v}_B\{A\}}{\bar{k}_B\bar{v}\{B_1\}} \quad (15)$$

with, in the case of equilibrium, $\{A\} = \{A\}_e$ and $\{B_1\} = \{B_1\}_e$.

2.3. Growth of the calcite surface

In this section, the process-based growth model for calcite is derived. A sketch illustrating the growth model is given in Fig. 3. A summary of the process-based model equations (subscript c) is given and compared to the corresponding Z&N model equations (subscript ZN) in Table 3; all symbols are defined in Appendix A. All equilibrium constant values are those for 25 °C and ambient pressure.

A step at the calcite surface advances or retreats through the addition or loss of calcium and (bi-)carbonate ions at growth sites. If P_A, P_{B_1}, and P_{B_2} are the probabilities of a kink site to be a calcium site $\equiv CO_3Ca^+$, a carbonate site $\equiv CaCO_3^-$ or a bicarbonate site $\equiv CaHCO_3^0$, then the net rates at which suitable ions are incorporated are

$$u_{A_1} = k_{A_1}\{A\}P_{B_1} - v_{A_1}P_A, \quad (16)$$

$$u_{A_2} = k_{A_2}\{A\}P_{B_2} - v_{A_2}P_A, \quad (17)$$

$$u_{B_1} = k_{B_1}\{B_1\}P_A - v_{B_1}P_{B_1}, \quad (18)$$

$$u_{B_2} = k_{B_2}\{B_2\}P_A - v_{B_2}P_{B_2}. \quad (19)$$

Combining Eqs. (16)–(19) with (9)–(12), and realizing that $P_{B_2} = 10^{8.6}\cdot10^{-pH}\cdot P_{B_1}$ (Table 1), gives

$$u_A = \bar{k}_A\{A\}P_{B_1} - \bar{v}_AP_A, \quad (20)$$

$$u_B = \bar{k}_B\{B_1\}P_A - \bar{v}_BP_{B_1}. \quad (21)$$

In order to maintain crystal stoichiometry, the net rates at which calcium and (bi-)carbonate ions are incorporated at kink sites must be equal. This means that the net rate of kink propagation (u_c) can be expressed as

$$u_A = u_B = \frac{1}{2}u_c. \quad (22)$$

If we define the fraction of potential growth sites as $\chi = (P_A + P_{B_1} + P_{B_2})$, from which it follows that $P_A = \chi - (1 + 10^{-pH}K_{\equiv CaHCO_3}P_{B_1} = \chi - \theta P_{B_1}$, then the propagation rate of a single kink can be derived by combining Eqs. (20)–(22) with (15):

$$u_c = 2\chi\bar{v}_A\bar{v}_B(S^2 - 1)\frac{1}{\bar{v}_A(Sr_i^{1/2} + \theta) + \bar{v}_B(\theta Sr_i^{-1/2} + 1)}\ (\text{in s}^{-1}) \quad (23)$$

where S is the saturation ratio for calcite:

$$S = \left[\frac{\{A\}\{B_1\}}{K_S}\right]^{1/2} = \left[\frac{\bar{k}_A\bar{k}_B\{A\}\{B_1\}}{\bar{v}_A\bar{v}_B}\right]^{1/2}, \quad (24)$$

Table 3
Summary of the key equations of the process-based growth model for calcite (index c), compared to the corresponding equations of the binary crystal growth model of Zhang and Nancollas (index ZN).

Process-based growth model summary
Kink propagation rate (in s^{-1})
$u_c = 2\chi\bar{\nu}_A\bar{\nu}_B(S^2-1)\frac{1}{\bar{\nu}_A\left(Sr_i^{1/2}+\theta\right)+\bar{\nu}_B\left(\theta Sr_i^{-1/2}+1\right)}$
$u_{ZN} = \nu(S^2-1)\frac{1}{S(r_i^{1/2}+r_i^{-1/2})/2+1}$
Kink formation rate (in s^{-1})
$i_c = \chi\bar{\nu}_A\bar{\nu}_B S(S^2-1)\exp(-2\epsilon/kT)\left(\frac{1}{\bar{\nu}_A r_i^{1/2}+\bar{\nu}_B S}+\frac{1}{\bar{\nu}_B r_i^{-1/2}+\bar{\nu}_A S}\right)$
$i_{ZN} = \nu S(S^2-1)\exp(-2\epsilon/kT)\left(\frac{1}{2}\right)\left(\frac{1}{r_i^{1/2}+S}+\frac{1}{r_i^{-1/2}+S}\right)$
Kink density
$\rho_c = S^{1/2}\exp(-\epsilon/kT)\left[\left(\frac{1}{\bar{\nu}_A S r_i^{1/2}+\bar{\nu}_B S}+\frac{1}{\bar{\nu}_B r_i^{-1/2}+\bar{\nu}_A S}\right)\Big/\left(\frac{1}{\bar{\nu}_A(Sr_i^{1/2}+\theta)+\bar{\nu}_B(\theta_S r_i^{-1/2}+1)}\right)\right]^{1/2}$
$\rho_{ZN} = 2S^{1/2}(S+1)\exp\left[\left(\frac{1}{r_i^{1/2}+S}+\frac{1}{r_i^{-1/2}+S}\right)\Big/\left(\frac{1}{S(r_i^{1/2}+r_i^{-1/2})/2+1}\right)\right]^{1/2}$
Growth rate (in s^{-1})
$R_c = \chi k_{in}(K_S\bar{k}_A\bar{k}_B)^{1/2}(S^2-1)S^{1/2}\ln S\left[\left(\frac{1}{\bar{\nu}_A r_i^{1/2}+\bar{\nu}_B S}+\frac{1}{\bar{\nu}_B r_i^{-1/2}+\bar{\nu}_A S}\right)\left(\frac{1}{\bar{\nu}_A(Sr_i^{1/2}+\theta)+\bar{\nu}_B(\theta Sr_i^{-1/2}+1)}\right)\right]^{1/2}$
$R_{ZN} = k_{in}(S^2-1)S^{-1/2}\ln S\left[\left(\frac{1}{r_i^{1/2}+S}+\frac{1}{r_i^{-1/2}+S}\right)\left(\frac{1}{S(r_i^{1/2}+r_i^{-1/2})+2)}\right)\right]^{1/2}$
With
$S = \left[\frac{\{A\}\{B_1\}}{K_S}\right]^{1/2} = \left[\frac{\bar{k}_A\bar{k}_B\{A\}\{B_1\}}{\bar{\nu}_A\bar{\nu}_B}\right]$ $\quad K_S = \frac{\bar{\nu}_A\bar{\nu}_B}{\bar{k}_A\bar{k}_B}$
$r_i = \frac{\bar{k}_A\bar{\nu}_B\{A\}}{\bar{k}_B\bar{\nu}_A\{B_1\}}$ $\quad k_{in} = \frac{2aK_S^{1/2}(\bar{k}_A\bar{k}_B)^{1/2}\exp(-\epsilon/kT)}{19\gamma/kT}$
$\chi = P_A + P_{B_1} + P_{B_2}$ $\quad \theta = (1+10^{-pH}K_{\equiv CaHCO_3})$

and r_i is expressed in terms of the activities of calcium and carbonate in the growth solution (Eq. (15)). If the effective detachment frequencies are equal, $\bar{\nu}_A = \bar{\nu}_B = \nu$, and all kink sites are suitable growth sites, and therefore $\chi = 1$, then Eq. (23) reduces to the kink propagation rate for a binary crystal obtained by Zhang and Nancollas (Table 3).

In order to use Eq. (23) to calculate growth rates, the density of growth sites needs to be known. Under supersaturated conditions, new kinks, or 1D clusters, are created mainly by addition of ions at non-kink positions along a step (Fig. 3). If a sufficiently elongated 1D cluster is formed by the attachment of additional ions, the cluster will be stable and two new kinks appear. Logically, both calcium and (bi-)carbonate sites can initiate a 1D cluster and overall stoichiometry during growth should be maintained. Following the approach of Zhang and Nancollas (1998), the rates of kink formation initiated on B kink sites (i_A) and A kink sites (i_B) are given by:

$$i_A = 2\chi\exp(-2\epsilon_A/kT)(S^2-1)\frac{\bar{k}_A\bar{\nu}_B\{A\}}{\bar{k}_A\{A\}+\bar{\nu}_B}, \quad (25)$$

$$i_B = 2\chi\exp(-2\epsilon_B/kT)(S^2-1)\frac{\bar{k}_B\bar{\nu}_A\{B_1\}}{\bar{k}_B\{B_1\}+\bar{\nu}_A}. \quad (26)$$

where ϵ is the energy to form an A (ϵ_A) or B (ϵ_B) kink site. As the overall rate of kink formation equals $i_c = (i_A + i_B)/2$, Eqs. (25) and (26), combined with Eqs. (15), (24), and the assumption $\epsilon_A = \epsilon_{B_1} = \epsilon_{B_2} = \epsilon$, lead to the following expression for the 1D nucleation rate:

$$i_c = \chi\bar{\nu}_A\bar{\nu}_B S\exp(-2\epsilon/kT)(S^2-1)\left(\frac{1}{\bar{\nu}_A r_i^{1/2}+\bar{\nu}_B S}+\frac{1}{\bar{\nu}_B r_i^{-1/2}+\bar{\nu}_A S}\right). \quad (27)$$

The rate of step advancement, V_c, can now be calculated using the net propagation rate of a single kink (u_c, Eq. (23)), and the steady state kink density (ρ_c) under supersaturated ($S > 1$) conditions (Zhang and Nancollas, 1998):

$$\rho_c = 2(i_c/2u_c)^{1/2} \quad (28)$$

$$V_c = \rho_c u_c a\,(\text{in m s}^{-1}) \quad (29)$$

where a is the closest spacing between calcium and carbonate ions in the lattice (3.199 Å). Further assuming that, for spiral growth, the surface is covered by parallel steps of equal spacing, y_0, the crystal growth rate, R_c, normal to the crystal surface is given by

$$R_c = aV_c/y_0\,(\text{in m s}^{-1}) \quad (30)$$

where, according to the Burton–Cabrera–Frank (BCF) theory of spiral growth,

$$y_0 = \frac{19a\gamma}{kT\ln S}\,(\text{in m}) \quad (31)$$

and γ represents the edge work (Burton et al., 1951).

3. MODEL PARAMETERS

The model parameters that must be specified in order to apply the process-based growth model are identified in Table 4. In this section, we derive values of the parameters

Table 4
Parameters of the process-based growth model. The literature ranges[a] are used as parameter constraints in the model calibration, see Section 3 in text for detailed discussion.

Parameter	Symbol	Process-based model value	Literature range[a]	References
Kink formation energy	ϵ, $\epsilon_{A,B}$	0.67×10^{-20} J	0.62–12×10^{-20} J	Zhang and Nancollas (1998) and Liang and Baer (1997)
Edge work	γ	1.2×10^{-19} J	1.0–13 $\times 10^{-20}$ J	Söhnel and Mullin (1982), Nielsen (1984), and Teng et al. (1998)
Attachment frequencies	k_{A_1}	8.5×10^{7} s^{-1}	$\sim 10^{5}$–10^{8} s^{-1}	Nielsen (1984) and Christoffersen and Christoffersen (1990)
	k_{A_2}	$\approx k_{A_1}$		This study
	k_{B_1}	$= 2k_{A_1} \frac{1+10^{8.6}10^{-pH}}{1+10^{10.33}10^{-pH}}$		This study
	k_{B_2}	$\approx k_{B_1}$		This study
Detachment frequencies	v_{A_1}	2.0×10^{3} s^{-1}	$< k_{A_1}$	This study
	v_{A_2}	$\approx v_{A_1}$		This study
	v_{B_1}	$= \frac{K_S \bar{k}_A \bar{k}_B}{\bar{\nu}(1+10^{8.6}10^{-pH})}$		This study
	v_{B_2}	$\approx \log v_{B_1}$		This study

by combining available constraints on the parameters with an optimization of the model step advancement rate (V_c, Eq. (29)) to AFM step velocities determined by Teng et al. (2000) and Stack and Grantham (2010). These data sets were selected because the solution conditions are well-defined. For most other published AFM data sets, including some experiments performed by Stack and Grantham (2010), we are only able to reproduce the solution chemistry after arbitrarily adjusting the pH or pCO_2 value. Any uncertainties in the actual pH or pCO_2 values during the AFM measurements affect the calculated values of S and χ, which result in large uncertainties in the model-calculated rates. The data of Teng et al. (2000) were collected at constant pH (8.5), ionic ratios r_{aq} close to 1, in NaCl background electrolyte and at variable degrees of supersaturation Ω (1–3.6). Those of Stack and Grantham (2010) were collected at $7 < pH < 9$, $10^{-3} < r_{aq} < 10^{3}$, in NaCl background electrolyte and at approximately constant degree of supersaturation Ω (2.2–2.7).

The kink formation energy (ϵ) is often assumed to have a value of $2kT = 6.2 \times 10^{-21}$ J in theoretical crystal growth rate calculations (Zhang and Nancollas, 1998). Burke and Nancollas (1999) used ϵ as a fitting parameter in their model and obtained values in the range 8.6–8.7 $\times 10^{-20}$ J for growth of octacalcium phosphate, and 14.6–26.0 $\times 10^{-20}$ J for dissolution of the same mineral phase. Liang and Baer (1997) calculated single kink formation energies from AFM data on a dissolving calcite surface and proposed a value of $9.8 \pm 1.8 \times 10^{-20}$ J. Here, we use the theoretical minimum of 6.2×10^{-21} J and assume that $\epsilon_A = \epsilon_B$. In the sensitivity analysis discussed below the value for ϵ is varied between the theoretical value of 6.2×10^{-21} J and the maximum value of 11.6×10^{-20} J reported by Liang and Baer (1997).

The edge work γ can be estimated using (Nielsen, 1984):

$$\gamma = kT[2.82 - 0.272 \ln(C_s)] \quad (32)$$

where C_s is the mineral solubility at equilibrium. For calcite, this implies that γ is slightly dependent on pH and pCO_2: for a pH range of 5–13 in a closed system, $\gamma = 1.5 \pm 0.2 \times 10^{-20}$ J, while for the same pH range in a system in equilibrium with the atmosphere, $\gamma = 0.9 \pm 0.3 \times 10^{-20}$ J. A slightly higher average value was reported by Kristensen et al. (2004) from molecular dynamic simulations of a calcite surface in vacuum: 1.85×10^{-10} J m^{-1} or 5.9×10^{-20} J (using the mean ionic diameter to recalculate to Joules). Söhnel and Mullin (1982) obtained a value of 1.0×10^{-20} J from experimental calcite nucleation data. Teng et al. (1998) reported the highest values estimated from *in situ* growth experiments in an AFM fluid cell for obtuse and acute steps. Their average recalculated value is 13×10^{-20} J. Here, we use the value obtained from Eq. (32) as initial estimate, while the lowest and highest reported values are used in the sensitivity analysis (see below).

According to Nielsen (1984), the attachment frequency of an ion is approximately 10^{-3} times its dehydration frequency when, following dehydration, the ion still has to diffuse from solution to a kink site. In our process-based model, however, the incorporation of a constituent ion corresponds to the transformation of an outer-sphere adsorbed calcium or (bi-)carbonate ion into an inner sphere complex with the accompanying removal of a water molecule. It is therefore expected that the attachment frequency is comparable to the dehydration frequency of the aqueous ion (about 10^{8} s^{-1} for calcium). Christoffersen and Christoffersen (1990) further noted that the surface lattice cations surrounding a kink site must be dehydrated for the anion to enter the site. If dehydration of surface cations is frequency determining for the attachment of anions, then the attachment frequency of the anions could be expected to be of the same order of magnitude as that of the cations.

The growth rate data of Nehrke et al. (2007; Fig. 1a) provide a further clue as to the relative attachment frequencies of cations and anions. For the conditions of each of the growth experiments, we computed the calcite surface speciation according to the calcite surface model presented in Table 1. As can be seen in Fig. 1b, the measured growth rates reach a maximum when the concentration ratio of (bi-) carbonate to calcium surface sites (Table 1) is approximately two. This suggests that under optimum growth conditions there are about twice as many attachment sites for calcium than for (bi-)carbonate ions, which further suggests a two-times slower attachment rate of calcium than

(bi-)carbonate. In what follows, the default assumption is therefore $\bar{k}_B = 2\bar{k}_A$.

Deprotonation of aqueous bicarbonate is very fast compared to the estimated attachment frequencies (6×10^9 M^{-1} s^{-1}; Jolley, 1984). Thus, it is reasonable to assume that deprotonation of surface bicarbonate ions does not have a significant effect on the attachment and detachment frequencies, that is, $k_{A_1} \approx k_{A_2}$, $k_{B_1} \approx k_{B_2}$, $v_{A_1} \approx v_{A_2}$, and $v_{B_1} \approx v_{B_1}$. To the authors' knowledge, no previously published growth model studies report detachment frequencies. It is often assumed that detachment frequencies are very small compared to attachment frequencies during mineral growth (Zhang and Nancollas, 1990). Here, the detachment frequency v_{A_1} is used as the only free fitting parameter, the other attachment and detachment frequencies are related as given in Table 4.

From the calcite surface model (Table 1, Wolthers et al., 2008), the amount of potential growth sites can be derived. For the experimental conditions under which Teng and coworkers and Stack and Grantham measured step velocities and Nehrke and coworkers measured single calcite crystal growth rates, the surface model yields growth site fractions χ on the order of 10^{-2}. In the rate calculations that follow, we impose the values of χ predicted by the CD-MUSIC model for the given experimental conditions. Note that this approach differs from that of Zhang and Nancollas (1998), who assume that all kink sites are potential growth sites (i.e., $\chi = 1$).

With the above constraints and initial parameter estimates, the process-based kinetic model is fitted to the step velocities of Teng et al. (2000) and Stack and Grantham (2010). (Note: some of the measured step velocities are excluded from the fit, due to uncertainties associated with the corresponding chemical compositions of the aqueous phase.) In the fitting procedure, model step velocities are computed for each individual set of experimental conditions, and the Residual Sum of Squares (RSS) between modeled and measured rates is minimized by adjusting model parameters γ, ϵ and k_{A_1}, within the respective ranges, as discussed above and given in Table 4, and by freely varying the value for detachment frequency v_{A_1} The resulting fit is shown in Fig. 4a and the corresponding set of parameter values is given in Table 4. As can be seen, the model is able to accurately reproduce the obtuse step velocities of Teng and coworkers and most of the step velocities reported by Stack and Grantham (2010). However, because the process-based growth model does not distinguish between different crystallographic orientations, it cannot account for the systematic differences in obtuse and acute step velocities measured with AFM (Fig. 4a). Further model developments aimed at reproducing the growing body of data on AFM step velocities will therefore have to separately represent the creation, densities and propagation of kink sites along acute and obtuse edges.

Additional published step velocities measured by AFM are compared in Fig. 4b to model-predicted step velocities. The figure shows that the model step velocities compare rather well with step velocities measured by Larsen et al. (2010), whose experimental conditions were similar to those of Teng et al. (2000) (see caption to Fig. 4) except for the background electrolyte, which was 0.1 M KCl rather than NaCl. The model overestimates the step velocities measured by Perdikouri et al. (2009) and Ruiz-Agudo et al. (2010) who worked at variable pH (7–11) and slightly higher

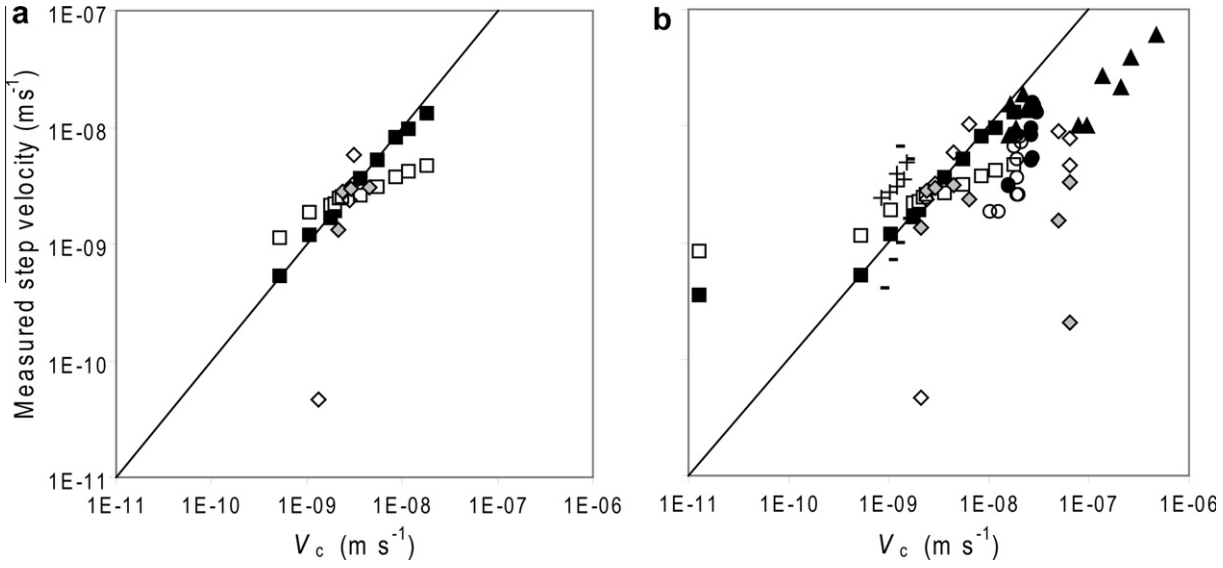

Fig. 4. (a) Model step velocities (V_c) calculated for the experimental conditions during measurements and optimized to fit the measured (■, ♦) obtuse and (□, ◇) acute step velocities on growing calcite surfaces observed with AFM at $r_{aq} \approx 1.0$, pH 8.5 at $1 < \Omega < 3.6$ (squares, Teng et al., 2000) and $7 <$ pH < 9, $10^{-3} < r_{aq} < 10^3$, in NaCl background electrolyte and $2.2 < \Omega < 2.7$ (diamonds, Stack and Grantham, 2010). Solid line indicates $x = y$. RSS is 1.1×10^{-19} m s^{-1}. Corresponding model parameters are given in Table 4. (b) Model step velocities (V_c) calculated for the experimental conditions during measurements of step velocities on growing calcite surfaces observed with AFM: for $2 \times 10^{-4} < r_{aq} < 2 \times 10^{+4}$ and pH 9.1–11.1 at (●) $\Omega = 6.4$ and (○) $\Omega = 5.2$ (Perdikouri et al., 2009); for $0.01 < r_{aq} < 10$ and pH 8.5 at $\Omega = 4$ for (−) acute and (+) obtuse step (Larsen et al., 2010); (▲) $r_{aq} = 1$, $\Omega = 6.5$ and varying pH (Ruiz-Agudo et al., 2010). Model step velocities were calculated using the parameters listed in Table 4. Solid line indicates $x = y$.

degrees of supersaturation in 0.1 M NaCl. Still, the trends in Fig. 4b tend to parallel the 1:1 line, implying that the model can account, at least in part, for the relative changes in step velocities under a wide range of chemical conditions.

3.1. Model sensitivity

The model-derived step velocities (V_c) and growth rates (R_c) are more sensitive to the kink formation energy (ϵ) than to the edge work (γ). When using the maximum value of ϵ (11.6×10^{-20} J), together with the minimum or maximum values of γ, the step velocities shown in Fig. 4a can not be fitted unless unrealistically high attachment frequencies are used ($>>10^{30}$ s^{-1}). In contrast, the minimum value for the kink formation energy (6.2×10^{-21} J) yields similarly good fits to the step velocities with both the minimum and maximum value for γ and realistic attachment frequencies.

As expected, the position of the growth rate optimum is sensitive to the ratio of $\bar{k}_B$ to $\bar{k}_A$ (Fig. 5). While the shape of the R_c versus $1/r_{aq}$ curve is unaffected by changes in the $\bar{k}_B : \bar{k}_A$ ratio, varying $\bar{k}_B : \bar{k}_A$ by one order of magnitude shifts the growth rate optimum by more than two orders of magnitude with respect to $1/r_{aq}$.

4. SOLUTION STOICHIOMETRY AND GROWTH RATES

The dependence of model-derived calcite crystal growth rates (R_c) on solution stoichiometry is illustrated in Fig. 6. The rates are calculated with the process-based growth model using the parameter values listed in Table 4, which were obtained from calibration on single step velocities measured at $7 < \text{pH} < 9$, $10^{-3} < r_{aq} < 10^{3}$, and $1 < \Omega < 3.6$. The results in Fig. 6a correspond to solution chemical conditions close to those in the single crystal growth experiments of Nehrke et al. (2007). The model yields rate maxima for solution activity ratios $r_{aq} \approx 1$, and near-symmetrical rate distributions that are only slightly dependent on the solution supersaturation. These model predictions are consistent with the observations of Nehrke et al. (compare Figs. 1a and 6a). Furthermore, the maximum growth rates predicted by the process-based model (7.2×10^{-11} m s^{-1} for Ω 16 ± 2 and 1.3×10^{-11} m s^{-1} for Ω 5.5 ± 0.5) are within order-of-magnitude agreement with the measured R_c values ($1.9 \pm 0.4 \times 10^{-11}$ m s^{-1} for Ω 16 ± 2 and $1.1 \pm 0.2 \times 10^{-11}$ m s^{-1} for Ω 5.5 ± 0.5). Taken together, these findings are quite remarkable, given that no model fitting to the growth rate measurements of Nehrke and coworkers is involved. That is, the model is able to scale from single step velocities up to single crystal growth rates.

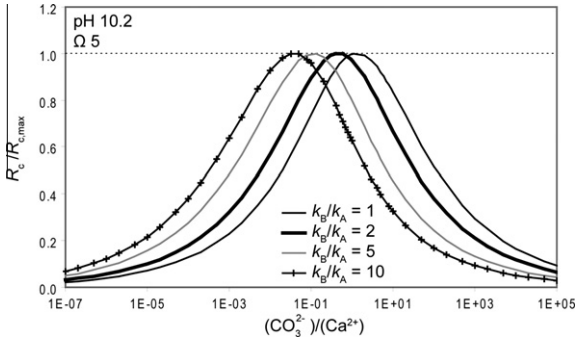

Fig. 5. Normalized process-based model rates at pH 10.2 and Ω 5 plotted against the solution activity ratio, for different ratios of attachment frequencies $\bar{k}_B$ versus $\bar{k}_A$.

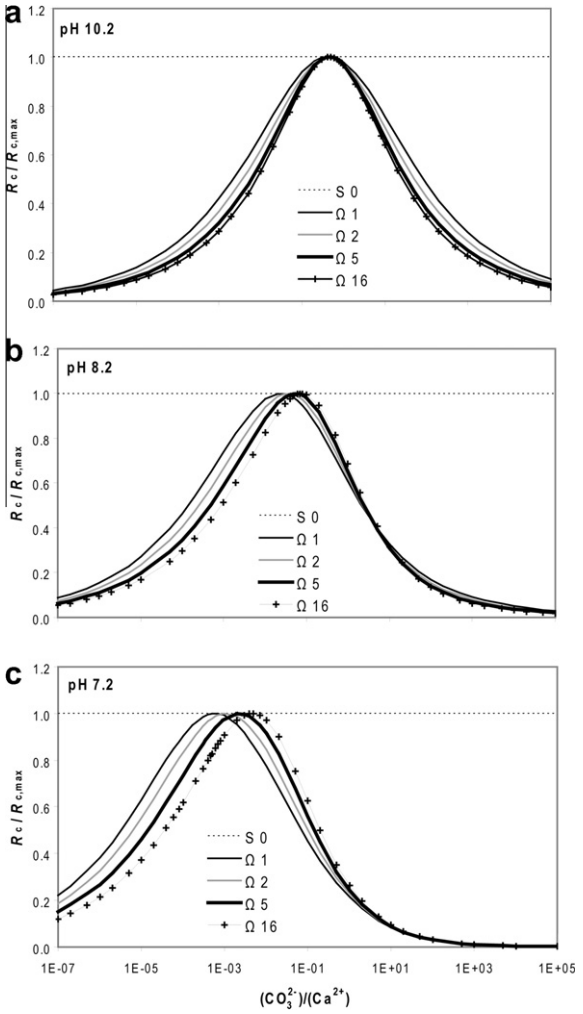

Fig. 6. Process-based model rates (R_c), normalized to maximum model rates ($R_{c,max}$), plotted for different degrees of supersaturation and (a) pH 10.2, (b) pH 8.2, (c) pH 7.2. Model rates for Ω 16 and 5 at pH 10.2 were calculated at the experimental conditions of Nehrke et al. (2007). Model rates were calculated using the parameter values listed in Table 4.

The results in Fig. 6 show that the position of the growth optimum and the shape of the rate distribution with respect to the solution activity ratio depend on pH. As pH decreases, aqueous carbonate ions become less abundant and growth increasingly relies on the attachment of bicarbonate ions (reaction 3.4 in Table 2). As a result, the growth optimum shifts to lower $1/r_{aq}$ values and the rate distribution becomes progressively more asymmetric. These trends are accentuated as the solution supersaturation decreases. Hence, from alkaline to neutral conditions, the functional dependence of calcite growth rates becomes

increasingly dependent on the degree of supersaturation. That is, the behavior of R_c with respect to solution stoichiometry becomes more complex at less alkaline conditions.

5. BULK CALCITE GROWTH RATES

In this section we assess to what extent the process-based growth model is able to reproduce bulk rates of calcite precipitation in seeded growth experiments. The sources of the published data sets used are identified in the caption of Fig. 7. The data comprises calcite growth rates measured at saturation ratios, $\Omega = IAP/K_s$, ranging from 1 to 33, pH values between 7.5 and 10, temperatures from 10 to 40 °C, in systems without or with a gas phase and, in the latter case, with pCO_2 values up to almost 800 times the atmospheric level and background electrolyte solution concentrations varying from uncontrolled ion strength to 0.001–0.7 M NaCl or KCl. Only rates measured in systems for which the chemical composition is completely known are used, because the aqueous and surface speciation are required to calculate the model growth rates. Additionally, only rates obtained in common background electrolyte solutions are used, since the current version of the CD-MUSIC model of the calcite surface cannot account for sorption of impurity ions. The model parameters are fixed to the values given in Table 4. It is important to note that these parameter values are independent of the measured rate data in Fig. 7: the only direct experimental rate data used to constrain the parameter values are the AFM step advancement rates of Teng et al. (2000) and Stack and Grantham (2010) as discussed in Section 3.

In Fig. 7a, the measured bulk calcite growth rates (R_c) are compared to the rates predicted by the process-based growth model. Although the plot exhibits significant scatter, most individual sets of measured rates fall either systematically above or below the 1:1 line. In addition, the trends defined by the data from the individual studies generally tend to parallel the 1:1 line, implying that the model reproduces the relative changes in growth rates under variable chemical conditions. It must be emphasized that the experimental growth rates were obtained under widely different experimental conditions, by different researchers using a variety of calcite seed materials and experimental approaches. The consistency of the trends suggests that the scatter in Fig. 7a reflects systematic differences among the individual rate data sets rather than a fundamental shortcoming of the process-based growth model.

The surface kink densities on which the model-calculated growth rates (R_c) in Fig. 7a are based are determined by the line density (ρ_c) and the step edge spacing (y_0) given by Eqs. (28) and (31), respectively. These equations are rooted in the classic Burton–Cabrera–Franck (BCF) crystal growth model and its derivatives (for a complete discussion, see Zhang and Nancollas, 1998). The calcite–water interface, however, is highly dynamic (Stipp and Hochella, 1991; Paquette and Reeder, 1995). Actual surface densities of growth sites could conceivably be lower, for example, when sites are blocked by impurities or step edges interact destructively, or higher, for example, when surface nucleation creates additional growth edges on the crystal surface (Kowacz et al., 2007) or when electrolyte ions interact with

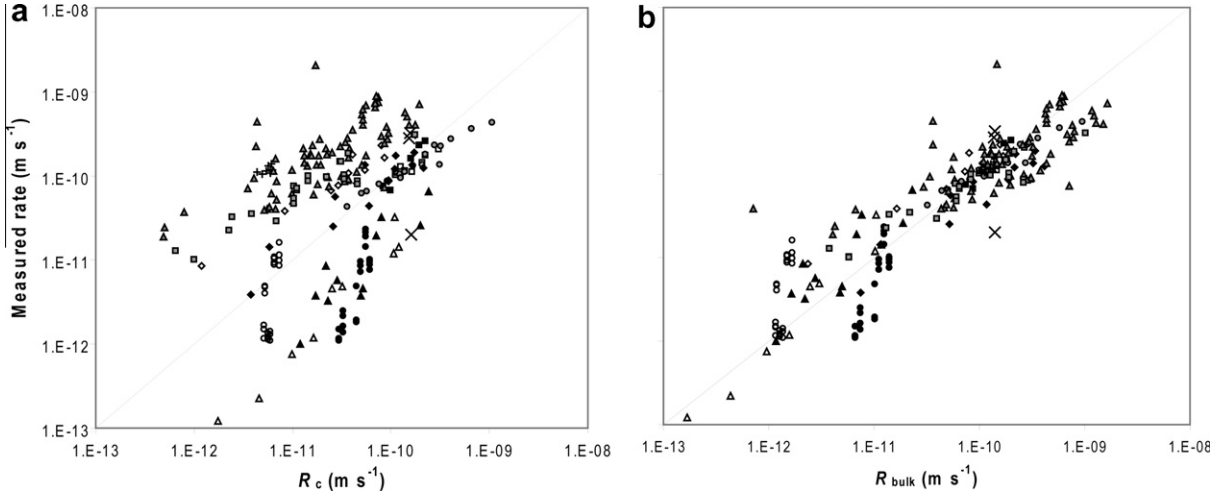

Fig. 7. (a) Measured bulk growth rate for calcite plotted versus process-based model rates calculated for the corresponding experimental conditions (RSS = 1.2×10^{-17} m s^{-1}). Measured growth rates: (●) Ω 16 ± 2 and (○) Ω 5–6 at pH 10.15 ± 0.05, no gas phase, I = 0.1 M NaCl and 20 ± 0.2 °C (Nehrke et al., 2007); (+) at Ω 4, I = 0.018 M NaCl and pH 9.5 (Tai et al., 2005); (♦) 1540 ppm CO_2, Ω 1.5–8.3 and (◇)310 ppm CO_2, Ω 1.7–9.8 (I = 0.07 M NaCl; Nilsson and Sternbeck, 1999); (▲) 30,500 Pa pCO_2 and (△) 2040 Pa pCO_2 (I = variable NaCl; Zuddas and Mucci, 1994); (△) variable Ω and pCO_2, pH 7.5 – 8.9 (I = 0.7 M KCl; van der Weijden et al., 1997); (□) pH 8.3–10 and T = 37 °C (I = variable; Christoffersen and Christoffersen, 1990); (□) pH 8.4 and variable pCO_2, (■) pH 8.2–8.7 at variable pCO_2, (○) pH 8.4 and variable ionic strength and (×) pH 8.4 and variable T (I = variable KCl; Inskeep and Bloom, 1985). The solid line indicates $x = y$. (b) Measured bulk growth rate for calcite plotted versus αR_c (Eq. (33)) calculated for the corresponding experimental conditions (RSS = 1.1×10^{-17} m s^{-1}). Symbols as in (a). Optimized values for logα are: (●) and (○) −0.64; (+) 1.36; (♦) and (◇) 0.30; (▲) and (△) −1.02; (△) 0.93; (□) 0.76; (□), (■), (○) and (×) −0.05.

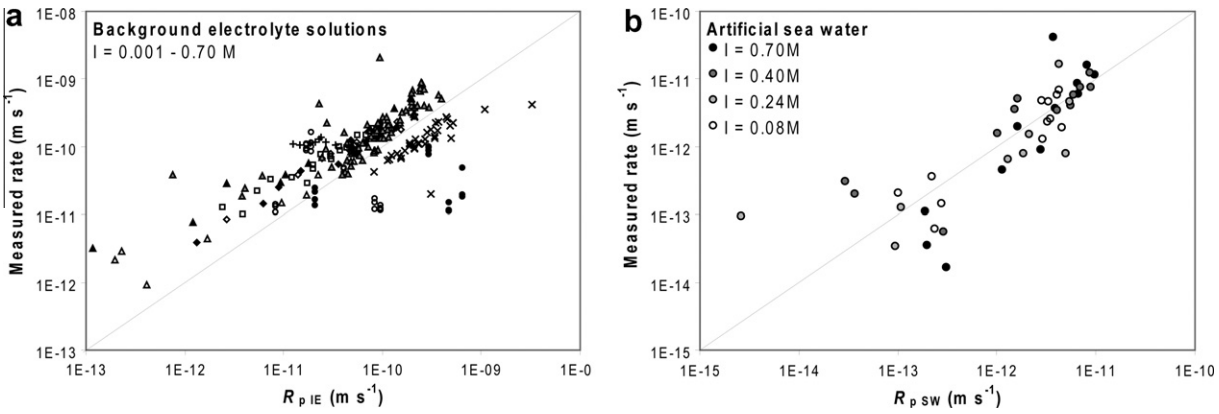

Fig. 8. (a) Measured bulk growth rate for calcite plotted versus rates calculated for the corresponding experimental conditions using: $R_{p\ BE} = I^{-0.004}\ pH^{-10.71} r_{aq}{}^{-0.35}\ (S-1)^2$ with $r_{aq} = \{Ca^{2+}\}/\{CO_3^{2-}\}$; RSS is 1.0×10^{-16} m s^{-1}. For symbol explanation see Fig. 7a. (b) Bulk growth rate for calcite measured in (diluted) artificial sea water (Zhong and Mucci, 1989) plotted versus rates calculated at exact experimental conditions using the parabolic rate law: $R_{p\ SW} = I^{0.36}\ pH^{-10.99} r_{aq}{}^{0.71}\ (S-2)^2$; RSS is 1.8×10^{-21} m s^{-1}. Solid lines indicate $x = y$.

the mineral surface (Fenter et al., 2010) or with dissolved constituent ions (Di Tommaso and de Leeuw, 2010).

In addition, the experimental linear growth rates plotted in Fig. 7a are obtained by dividing the measured mass of calcite precipitated per unit time by the surface area of the seed crystals. Specific surface areas are estimated based on experimental data (e.g., BET isotherms) or geometrical considerations. These approaches only incompletely account for variations in the surface microtopography of mineral surfaces (e.g., Dzombak and Morel, 1990; Dixit and Van Cappellen, 2002; Wolthers et al., 2003). Hence, we suspect that variations in the microscopic surface roughness of calcite seed crystals may be a major source of the scatter between the individual studies observed in Fig. 7a.

In order to account for possible deviations from the theoretical kink surface densities and the uncertainties associated with estimates of the specific surface areas of the calcite seed crystals, we introduce a non-dimensional surface roughness correction factor, α, so that

$$R_{measured} = \alpha \cdot R_c \tag{33}$$

where for any given experimental growth study the value of α is fixed, while it is allowed to vary from one study to another. As can be seen in Fig. 7b, using α as the only adjustable parameter, it is possible to reconcile the large body of measured bulk growth rates of calcite with the process-based model.

The values of $\log \alpha$ obtained by fitting the measured bulk growth rates to Eq. (33) range from -1.02 to 1.36 (Fig. 7b). Further interpretation of this large variation in α will require detailed characterization of the surfaces of calcite seed crystals. That such large differences in α occur even among seeded growth experiments carried out under controlled laboratory conditions in common background electrolyte solutions point to the inherent difficulties associated with extrapolating laboratory rates of calcite growth to natural environments. This reactive-surface-area problem represents a recurrent challenge in geochemical mineral–water interactions (e.g., Velbel, 1985; White and Peterson, 1990; Van Cappellen, 1996; White and Brantley, 2003; Jourabchi et al., 2008; Pallud et al., 2010).

6. EMPIRICAL GROWTH RATE EQUATIONS

The previous section shows that a diverse set of bulk calcite growth rates, obtained independently for a wide range of chemical conditions, can be successfully described by the process-based model. Nevertheless, the implementation of the model for routine geochemical modeling may be quite cumbersome. Furthermore, due to the introduction of the empirical correction factor α, the applicability of the process-based growth model as a predictive tool for calcite growth rates is limited as long as the value for α for a particular system is unknown. For practical applications, we therefore derive an empirical growth rate expression using the same set of bulk growth rate data as in Fig. 7. Additionally, we derive an empirical growth rate expression for growth in seawater-type solutions. Both expressions assume a parabolic dependency of the calcite growth rate on the degree of supersaturation (Nielsen, 1981) and explicitly accounts for additional effects of ionic strength, solution stoichiometry and pH.

The following parabolic rate law describes the calcite growth rate observed in experiments with common background electrolyte solutions ($I = 0.001$–0.7 M):

$$R_{p\ BE} = I^{-0.004} pH^{-10.71} r_{aq}^{-0.35} (S-1)^2 \tag{34}$$

where I is the ionic strength, $r_{aq} = \{Ca^{2+}\}/\{CO_3^{2-}\}$ activity ratio, S is the saturation ratio ($\Omega^{1/2}$), and $R_{p\ BE}$ is expressed in m s^{-1}. (Note that linear growth rates can be converted to rates in units of mass per unit surface area and per unit time via the molecular density of calcite, 2.71×10^4 mol m^{-3}.) As can be seen in Fig. 8a, the rate equation provides a reasonably good description of the measured rates.

A second parabolic rate law is derived for calcite growth in seawater-type solutions. It is based on the calcite growth rates of Zhong and Mucci (1989) measured in undiluted and diluted artificial seawater solutions ($I = 0.08$–0.7 M). These growth rates are orders of magnitude lower than

rates obtained at similar degrees of supersaturation in background electrolyte solutions. The rates are described by the following parabolic rate law (Fig. 8b):

$$R_{p\ SW} = I^{0.36}\mathrm{pH}^{-10.99} r_{aq}^{0.71}(S-2)^2 \quad (35)$$

where $R_{p\ SW}$ is expressed in m s^{-1}. Comparison of Eqs. (34) and (35) implies a stronger dependency of calcite growth rate on ionic strength in seawater-type solutions. Mainly this reflects the presence of growth inhibiting ions such as magnesium, sulfate and phosphate in the artificial seawater solutions.

7. CONCLUSIONS

A new, process-based rate model for the crystal growth of calcite from aqueous solution is presented. The model combines kinetic descriptions of the incorporation of calcium, carbonate and bicarbonate ions at kink sites along step edges, with equilibrium calculations of the surface chemical structure of the calcite–solution interface under variable aqueous chemical conditions. Key model parameters are calibrated by fitting the model to a selected set of step velocities on calcite surfaces measured by AFM. Without any further adjustment of the parameter values, the model reproduces the observed dependence of the macroscopic growth rate of single calcite crystals on the solution activity ratio of calcium and carbonate ions ($r_{aq} = \{Ca^{2+}\}/\{CO_3^{-2}\}$) under alkaline conditions. In order to reconcile the model with bulk precipitation rates measured in seeded growth experiments a surface roughness factor is introduced. The latter accounts for deviations of the calcite kink density from the theoretical density based on the classical BCF theory of spiral growth, but also for uncertainties associated with specific surface area estimations. Constraining the effective concentration of growth sites remains one of the main obstacles to the extrapolation of molecular-scale crystal growth models to mineral precipitation rates in geochemical field systems.

ACKNOWLEDGEMENTS

We would like to thank the associate editor, Dimitri Sverjensky, an anonymous reviewer and Adrián Villegas-Jiménez for their insightful reviews. Financial support from the Netherlands Organisation for Scientific Research (NWO) through VENI Grant #863.06.006 to M.W. and from the Darwin Centre for Biogeosciences is acknowledged. G.N. was supported by the DFG Grant NE 1564/1-1 (SPP1158). This is publication number DW-2011-1001 of the Darwin Center for Biogeosciences.

A	(index for) calcium ion
{A}	activity of calcium ion
A_1, A_2	index for a calcium ion reacting with a carbonate or bicarbonate surface site, respectively
a	mean ionic diameter (3.199 Å for calcite)
B	(index for) carbonate and bicarbonate ions (see Eqs. (10) and (12))
B_1	(index for) carbonate ion
$\{B_1\}$	activity of carbonate ion
B_2	(index for) bicarbonate ion
$\{B_2\}$	activity of bicarbonate ion
BE	index for parabolic rate law in common background electrolyte solutions
c	index for process-based calcite growth model
C_s	mineral solubility at equilibrium (Eq. (32) only)
e	index for equilibrium
IAP	Activity product of the constituent ions, $\{Ca^{2+}\}\{CO_3^{-2}\}$ for calcite
K_S	solubility product of calcite (Eq. (1))
K_{S_H}	solubility product of calcite in terms of $\{Ca^{2+}\}$ and $\{HCO_3^2\}$ (Eq. (2))
k	Boltzmann constant
k_{A_1}, k_{A_2}, k_{B_1}, k_{B_2}	attachment frequencies for A_1, A_2, B_1 and B_2 ions
$\overline{k_A}$, $\overline{k_B}$	overall attachment frequencies for calcium and (bi-) carbonate
NS	(index) for Nilsson and Sternbeck (1999)
P	probability
p	index for parabolic rate law
R	overall growth rate
r_{aq}	ionic activity ratio $\{Ca^{2+}\}/\{CO_3^{2-}\}$
r_i	kinetic ionic ratio for integration (Eq. (15))
RSS	residual sum of squares
S	saturation ratio $((IAP/K_s)^{1/2} = \Omega^{1/2}$
S_{tot}	total number of surface sites
SW	index for parabolic rate law in seawater type solutions
T	temperature
u	kink propagation rate
V	rate of step movement
ZN	(index for) Zhang and Nancollas (1998)
y_0	step spacing in a spiral
α	surface roughness factor (Eq. (33))
γ	edge work
Δz_0, Δz_1	Boltzmann parameters for surface reactions (Table 1 only)
ϵ	kink formation energy
θ	term for speciation between carbonate and bicarbonate
ν_{A_1}, ν_{A_2}, ν_{B_1}, ν_{B_2}	detachment frequencies for A, B_1 and B_2 ions
$\overline{\nu_A}$, $\overline{\nu_B}$	overall detachment frequencies for calcium and (bi-) carbonate
ξ	$=\exp(-2\varepsilon/kT)$
ρ	kink density
χ	fraction of growth sites at the surface
Ω	saturation ratio (IAP/K_s)
$\equiv_c$, $\equiv_e$, $\equiv_f$	corner site, edge site or face site at the calcite surface

APPENDIX A. NOMENCLATURE

See also Table 4.

REFERENCES

Arakaki T. and Mucci A. (1995) A continuous and mechanistic representation of calcite reaction-controlled kinetics in dilute solutions at 25 °C and 1 atm total pressure. *Aquat. Geochem.* **1**, 105–130.

Burke E. M. and Nancollas G. H. (1999) Relation of lattice ion solution composition to octacalcium phosphate dissolution kinetics. *Colloids Surf. A* **150**, 151–160.

Burton W. K., Cabrera N. and Frank F. C. (1951) The growth of crystals and the equilibrium structure of their surfaces. *Philos. Trans. R. Soc. London A* **243**, 299–358.

Chernov A. A., Petrova E. V. and Rashkovich L. N. (2006) Dependence of the CaOx and MgOx growth rate on solution stoichiometry. Non-Kossel crystal growth. *J. Cryst. Growth* **289**, 245–254.

Christoffersen J. and Christoffersen M. R. (1979) Kinetics of dissolution of calcium hydroxyapatite. II. Dissolution in non-stoichiometric solutions at constant pH. *J. Cryst. Growth* **47**, 671–679.

Christoffersen J. and Christoffersen M. R. (1990) Kinetics of spiral growth of calcite crystals and determination of the absolute rate constant. *J. Cryst. Growth* **100**, 203–211.

Davies C. W. and Jones A. L. (1955) The precipitation of silver chloride from aqueous solutions: part 2. – kinetics of growth of seed crystals. *Trans. Faraday Soc.* **51**, 812–817.

Davies C. W. and Nancollas G. H. (1955) The precipitation of silver chloride from aqueous solutions: part 3. – temperature coefficients of growth and solution. *Trans. Faraday Soc.* **51**, 818–823.

De Leeuw N. H. and Parker S. C. (1998) Surface structure and morphology of calcium carbonate polymorphs calcite, aragonite, and vaterite: an atomistic approach. *J. Phys. Chem. B* **102**, 2914–2922.

Di Tommaso D. and de Leeuw N. H. (2010) First principles simulations of the structural and dynamical properties of hydrated metal ions Me^{2+} and solvated metal carbonates (Me = Ca, Mg, and Sr). *Cryst. Growth Des.* **10**, 4292–4302.

Dixit S. and Van Cappellen P. (2002) Surface chemistry and reactivity of biogenic silica. *Geochim. Cosmochim. Acta* **66**, 2559–2568.

Dzombak D. A. and Morel F. M. M. (1990) *Surface complexation modelling, hydrous ferric oxide*. Wiley & Sons, New York.

Fenter P., Lee S. S., Park C., Catalano J. G., Zhang Z. and Sturchio N. C. (2010) Probing interfacial reactions with X-ray reflectivity and X-ray reflection interface microscopy: influence of NaCl on the dissolution of orthoclase at pOH 2 and 85 °C. *Geochim. Cosmochim. Acta* **74**, 3396–3411.

Gustafsson J. P. (2008) *Visual MINTEQ Version 2.52*. Stockholm, Sweden.

Hiemstra T. and Van Riemsdijk W. H. (1996) A surface structural approach to ion adsorption: the charge distribution (CD) model. *J. Colloid Interf. Sci.* **179**, 488–508.

Hiemstra T., Venema P. and Van Riemsdijk W. H. (1996) Intrinsic proton affinity of reactive surface groups of metal (hydr)oxides: the bond valence principle. *J. Colloid Interf. Sci.* **184**, 680–692.

Hofmann A. F., Middelburg J. J., Soetaert K., Wolf-Gladrow D. A. and Meysman F. J. R. (2010) Proton cycling, buffering, and reaction stoichiometry in natural waters. *Mar. Chem.* **121**, 246–255.

Inskeep W. P. and Bloom P. R. (1985) An evaluation of rate equations for calcite precipitation kinetics at pCO_2 less than 0.01 atm and pH greater than 8. *Geochim. Cosmochim. Acta* **49**, 2165–2180.

Jolley W. L. (1984) *Modern Inorganic Chemistry*. McGraw-Hill, NY, p. 194.

Jourabchi P., Meile C., Pasion L. R. and Van Cappellen P. (2008) Quantitative interpretation of pore water O_2 and pH distributions in deep-sea sediments. *Geochim. Cosmochim. Acta* **72**, 1350–1364.

Kossel W. (1930) Uber Krystallwachstum. *Die Naturwissenschaften* **18**, 901–910.

Kowacz M., Putnis C. V. and Putnis A. (2007) The effect of cation:anion ratio in solution on the mechanism of barite growth at constant supersaturation: Role of the desolvation process on the growth kinetics. *Geochim. Cosmochim. Acta* **71**, 5168–5179.

Kristensen R., Stipp S. L. S. and Refson K. (2004) Modeling steps and kinks on the surface of calcite. *J. Chem. Phys.* **121**, 8511–8523.

Larsen K., Bechgaard K. and Stipp S. L. S. (2010) Modelling spiral growth at dislocations and determination of critical step lengths from pyramid geometries on calcite {1 0–1 4} surfaces. *Geochim. Cosmochim. Acta* **74**, 558–567.

Lasaga A. C. (1998) *Kinetic theory in the earth sciences*. Princeton U.P., New Jersey.

Liang Y. and Baer D. R. (1997) Anisotropic dissolution at the $CaCO_3$(1014) – water interface. *Surf. Sci.* **373**, 275–287.

Morse J. W., Arvidson R. S. and Lüttge A. (2007) Calcium carbonate formation and dissolution. *Chem. Rev.* **107**, 342–381.

Nehrke G., Reichart G. J., Van Cappellen P., Meile C. and Bijma J. (2007) Dependence of calcite growth rate and Sr partitioning on solution stoichiometry: non-Kossel crystal growth. *Geochim. Cosmochim. Acta* **71**, 2240–2249.

Nielsen A. E. (1981) Theory of electrolyte crystal growth. The parabolic rate law. *Pure Appl. Chem.* **53**, 2025–2039.

Nielsen A. E. (1984) Electrolyte crystal growth mechanisms. *J. Cryst. Growth* **67**, 289–310.

Nielsen A. E. and Toft J. M. (1984) Electrolyte crystal growth kinetics. *J. Cryst. Growth* **67**, 278–288.

Nilsson O. and Sternbeck J. (1999) A mechanistic model for calcite crystal growth using surface speciation. *Geochim. Cosmochim. Acta* **63**, 217–225.

Pallud C., Kausch M., Fendorf S. and Meile C. (2010) Spatial patterns and modeling of reductive ferrihydrite transformation observed in artificial soil aggregates. *Environ. Sci. Technol.* **44**, 74–79.

Paquette J. and Reeder R. J. (1995) Relationship between surface structure, growth mechanism, and trace element incorporation in calcite. *Geochim. Cosmochim. Acta* **59**, 735–749.

Perdikouri C., Putnis C. V., Kasioptas A. and Putnis A. (2009) An atomic force microscopy study of the growth of a calcite surface as a function of calcium/total carbonate concentration ratio in solution at constant supersaturation. *Cryst. Growth Des.* **9**, 4344–4350.

Plummer L. N. and Busenberg G. E. (1982) The solubilities of calcite, aragonite and vaterite in CO_2–H_2O solutions between 0 and 90 °C and an evaluation of the aqueous model for the system $CaCO_3$–CO_2–H_2O. *Geochim. Cosmochim. Acta* **46**, 1011–1040.

Plummer L. N., Wigley T. M. L. and Parkhurst D. L. (1978) Kinetics of calcite dissolution in CO_2 – water systems at 5 degree to 60 degree C and 0.0 to 1.0 atm CO_2. *Am. J. Sci.* **278**, 179–216.

Pokrovsky O. S. and Schott J. (2002) Surface chemistry and dissolution kinetics of divalent metal carbonates. *Environ. Sci. Technol.* **36**, 426–432.

Pokrovsky O. S., Golubev S. V. and Schott J. (2005) Dissolution kinetics of calcite, dolomite and magnesite at 25 °C and 0 to 50 atm pCO_2. *Chem. Geol.* **217**, 239–255.

Rashkovich L. N., De Yoreo J. J., Orme C. A. and Chernov A. A. (2006) In situ atomic force microscopy of layer-by-layer crystal growth and key growth concepts. *Crystallogr. Reports* **51**, 1063–1074.

Reddy M. M., Plummer L. N. and Busenberg E. (1981) Crystal growth of calcite from calcium bicarbonate solutions at constant pCO_2 and 25 °C: a test of a calcite dissolution model. *Geochim. Cosmochim. Acta* **45**, 1281–1289.

Ruiz-Agudo E., Putnis C. V., Rodriguez-Navarro C. and Putnis A. (2010) Effect of pH on calcite growth at constant $a_{Ca^{2+}}/a_{CO_3^{2-}}$ ratio and supersaturation. *Geochim. Cosmochim. Acta* **75**, 284–296.

Söhnel O. and Mullin J. W. (1982) Precipitation of calcium carbonate. *J. Cryst. Growth* **60**, 239–250.

Stack A. G. and Grantham M. C. (2010) Growth rate of calcite steps as a function of aqueous calcium-to-carbonate ratio: independent attachment and detachment of calcium and carbonate ions. *Cryst. Growth Des.* **10**, 1414–1418.

Stipp S. and Hochella M. F. (1991) Structure and bonding environments at the calcite surface as observed with X-ray photoelectron spectroscopy (XPS) and low energy electron diffraction (LEED). *Geochim. Cosmochim. Acta* **55**, 1723–1736.

Stubičar N., Ščrbak M. and Stubičar M. (1990) Crystal growth of lead fluoride using the constant composition method II. The effect of Pb/F activity ratio on the kinetics of crystal growth. *J. Cryst. Growth* **100**, 261–267.

Tai C. Y., Lu J.-. and Wu J.-. (2005) Crystal growth rate of calcite in a constant-composition environment. *J. Chin. Inst. Chem. Eng,* **36**, 443–450.

Teng H. H., Dove P. M., Orme C. A. and De Yoreo J. J. (1998) Thermodynamics of calcite growth: baseline for understanding biomineral formation. *Science* **282**, 724–727.

Teng H. H., Dove P. M. and DeYoreo J. J. (2000) Kinetics of calcite growth: surface processes and relationships to macroscopic rate laws. *Geochim. Cosmochim. Acta* **64**, 2255–2266.

Van Cappellen P. (1996) Reactive surface area control of the dissolution kinetics of biogenic silica in deep-sea sediments. *Chem. Geol.* **132**, 125–130.

Van Cappellen P., Charlet L., Stumm W. and Wersin P. (1993) A surface complexation model of the carbonate mineral–aqueous solution interface. *Geochim. Cosmochim. Acta* **57**, 3505–3518.

Van der Weijden R. D., van der Weijden A. E., Witkamp G. J. and van Rosmalen G. M. (1997) The influence of total calcium and total carbonate on the growth rate of calcite. *J. Cryst. Growth* **171**, 190–196.

Velbel M. A. (1985) Geochemical mass balances and weathering rates in forested watersheds of the southern Blue Ridge. *Am. J. Sci.* **285**, 904–930.

Verbeeck R. M. H. and Devenyns J. A. H. (1990) The effect of the solution Ca/P ratio on the kinetics of dissolution of octacalcium phosphate at constant pH. *J. Cryst. Growth* **102**, 647–657.

Verbeeck R. M. H. and Devenyns J. A. H. (1992) The kinetics of dissolution of octacalcium phosphate II. The combined effects of pH and solution Ca/P ratio. *J. Cryst. Growth* **121**, 335–348.

White A. F. and Brantley S. L. (2003) The effect of time on the weathering of silicate minerals: why do weathering rates differ in the laboratory and field? *Chem. Geol.* **202**, 479–506.

White A. F. and Peterson M. L. (1990) Role of reactive-surface-area characterization in geochemical kinetic models. In Chemical Modeling of Aqueous Systems II. *ACS Sym. Ser.* **416**, 461–475.

Wolthers M., van der Gaast S. J. and Rickard D. (2003) The structure of disordered mackinawite. *Am. Mineral.* **88**, 2007–2015.

Wolthers M., Charlet L. and Van Cappellen P. (2008) The surface chemistry of divalent metal carbonate minerals; a critical assessment of surface charge and potential data using the charge distribution multi-site ion complexation model. *Am. J. Sci.* **308**, 905–941.

Zhang J. and Nancollas G. H. (1990) Kink densities along a crystal surface step at low temperatures and under nonequilibrium conditions. *J. Cryst. Growth* **106**, 181–190.

Zhang J. and Nancollas G. H. (1992) Influence of calcium/sulfate molar ratio on the growth rate of calcium sulfatedihydrate at constant supersaturation. *J. Cryst. Growth* **118**, 287–294.

Zhang J. and Nancollas G. H. (1998) Kink density and rate of step movement during growth and dissolution of an AB crystal in a nonstoichiometric solution. *J. Colloid Interf. Sci.* **200**, 131–145.

Zhong S. and Mucci A. (1989) Calcite and aragonite precipitation from seawater solutions of various salinities: precipitation rates and overgrowth compositions. *Chem. Geol.* **78**, 283–299.

Zuddas P. and Mucci A. (1994) Kinetics of calcite precipitation from seawater: I. A classical chemical kinetics description for strong electrolyte solutions. *Geochim. Cosmochim. Acta* **58**, 4353–4362.

Associate editor: Dimitri A. Sverjensky